ACS MATERIALS LETTERS

www.acsmaterialsletters.org

Letter

Metal-Organic Coordination Nanotubes as Advanced Architectures for Efficient Ammonia Electrosynthesis via Pure Nitrate Reduction in Neutral Media

Miao Wang,[#] Qian Teng,[#] Qianchuan Yu,[#] Heng Zhou,[#] Shuaikang Yang, Tianyu Shen,* Huaizhu Wang, Zuoao Wu, Zuoxiu Tie,* Shuangming Chen,* Li-Min Zheng,* and Zhong Jin*

Cite This: https://doi.org/10.1021/acsmaterialslett.6c00317

Read Online

ACCESS | Metrics & More | Article Recommendations | Supporting Information

ABSTRACT: Metal-organic coordination materials have emerged as promising candidates for electrocatalytic nitrate reduction reaction (NITRR), but the molecular-level engineering required for constructing high-efficiency electrocatalysts remains challenging. This study addresses this gap by developing a class of metal-organic coordination nanotubes (MONTs) as atomically precise single-site electrocatalysts, including **Fe-MONTs**, **Co-MONTs**, and **Ni-MONTs**. Benefited from the unique coordination structure, the **Co-MONT** electrode exhibited superior electrocatalytic performances for the NITRR, achieving an ammonia production Faradaic efficiency of 89.9% at −0.7 V (vs reversible hydrogen electrode) and an ammonia yield rate of 231.3 mmol h^{-1} $g^{-1}_{cat.}$ in pure nitrate solution. Through combining in situ characterizations and theoretical simulations, the electrocatalysis mechanisms and active site configurations were elucidated. This work establishes MONTs as an intriguing platform for electrochemical wastewater purification and sustainable ammonia synthesis, providing promising design principles for advanced electrocatalysts.

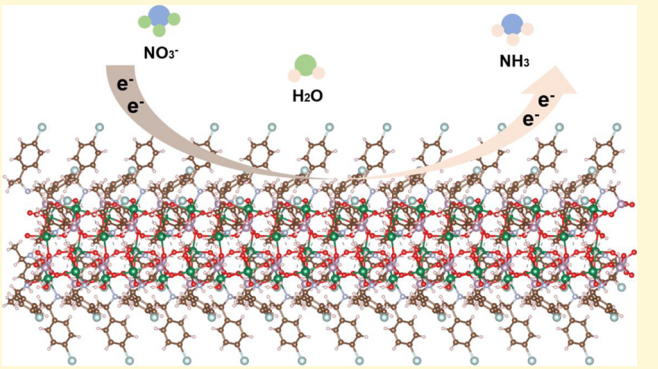

Ammonia (NH_3) is a vital industrial chemical with widespread applications in chemical manufacturing, agriculture, pharmaceuticals, and renewable energy technologies.[1,2] Currently, NH_3 production predominantly relies on the energy-intensive Haber−Bosch process, which operates under extreme conditions (400–500 °C, 100–300 atm) and depends on hydrogen derived from fossil fuel reforming, resulting in substantial CO_2 emissions.[3] Given these limitations, developing sustainable NH_3 synthesis methods has become a critical research focus. Electrocatalytic conversion of nitrogenous molecules (e.g., N_2 and NO_3^-) into NH_3 under ambient conditions has recently gained attention as a promising alternative. While extensive studies have explored N_2 electroreduction, its practical application remains hindered by the extreme stability of the N≡N triple bond (dissociation energy 941 kJ mol^{-1}) and the low solubility of N_2 in aqueous electrolytes.[4−8] In contrast, nitrate (NO_3^-) reduction offers faster reaction kinetics due to the weaker N=O bond (204 kJ mol^{-1}) and higher solubility in water.[9−13] Beyond its potential for NH_3 synthesis, NO_3^- is a major environmental pollutant linked to carcinogenic nitrosamine formation in ecosystems.[14] Rising nitrate levels in groundwater, largely due to anthropogenic activities, further underscore the urgency of effective remediation strategies. The electrocatalytic nitrate reduction (NITRR) presents a dual opportunity for concurrent sustainable NH_3 production and environmental purification. However, challenges such as intricate proton-coupled electron transfer processes and restricted reaction kinetics caused by intermediate species continue to hamper its practical implementation.

Despite their effectiveness in the NITRR, noble metal (e.g., Rh, Ru, Pd, Ir) and alloy electrocatalyts face limitations due to scarcity and prohibitive costs.[15,16] This has spurred extensive research into transition metal alternatives (e.g., Fe, Co, Ni, Cu, Zn) that offer comparable activity at substantially lower expense.[17,18] Furthermore, recent attention has shifted to atomically precise single-site catalysts, which offer distinct advantages including fully exposed active sites, uniform coordination environments, high specific surface areas, near-100% metal utilization efficiency, efficient charge/mass transport, and tunable electronic/catalytic properties,[19−24] but still lack a universal molecular-level engineering methodology for designing

Received: March 27, 2026
Revised: June 25, 2026
Accepted: June 25, 2026

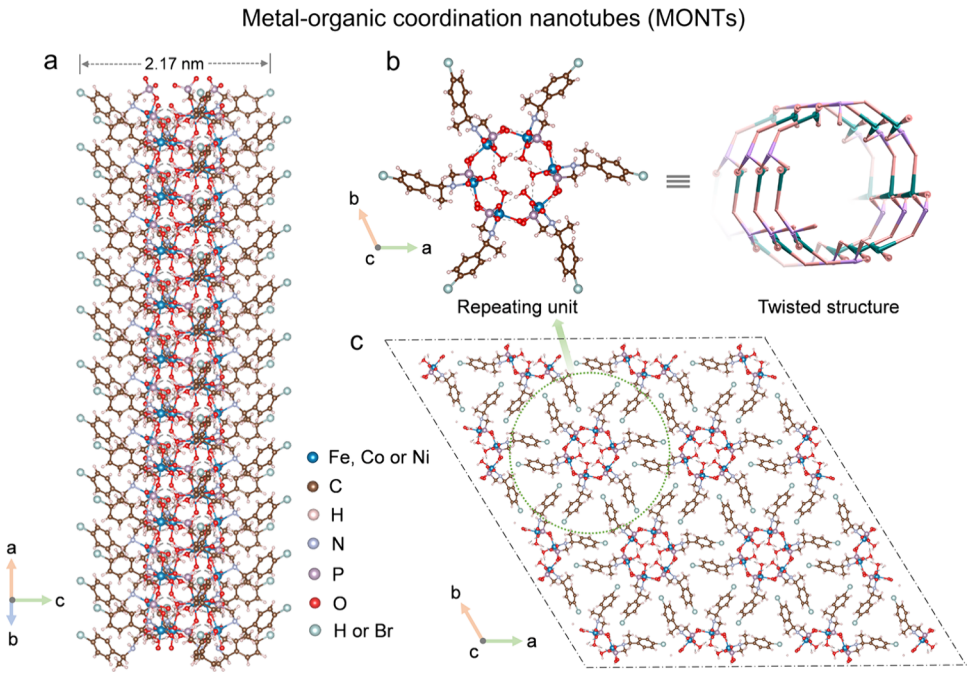

Figure 1. Schematic diagrams of (a) side-view and (b, c) top-view crystalline structures of MONTs.

next-generation electrocatalysts. Notably, in real-world applications, ensuring the consistent performance of catalysts in neutral effluent is essential, as introducing pH-adjusting agents would disrupt the optimal balance between costs and profits in industrial-scale treatment processes. However, in neutral environments, the limited availability of active hydrogen (*H) on the electrode surface at low overpotentials severely hampers the NH_3 hydrogenation efficiency, leading to diminished production rates and poor NH_3 selectivity. Another challenge lies in achieving high ammonia production Faradaic efficiency (FE_{NH3}) and ammonia yields from pure nitrate sources while simultaneously generating sufficiently concentrated ammonia solutions to minimize downstream separation costs.

Herein, we report a precision-engineered molecular design strategy enabling the synthesis of a family of metal-organic coordination nanotubes (MONTs) exhibiting unprecedented catalytic efficacy for the nitrogen reduction reaction (NITRR). Three distinct variants were successfully fabricated: *R*-[Fe(pemp)$(H_2O)_2$] (**Fe-MONTs**), *R*-[Co(Brpemp)$(H_2O)_2$] (**Co-MONTs**), and *R*-[Ni(pemp)$(H_2O)_2$]·1/3CH_3CN (**Ni-MONTs**). Thess architectures are constructed through coordination-driven self-assembly of [M-O_5N] octahedral building blocks interconnected by phosphonate-functionalized [P-O_3C] tetrahedral linkers, yielding tubular frameworks with tunable pore environments, optimized active site accessibility, and synergistic electronic modulation for enhanced electrocatalytic performance. Among them, the **Co-MONTs** electrode exhibited peak activity, delivering a FE_{NH3} of 89.9% at −0.7 V (vs RHE) in pure 0.5 M KNO_3 solution while achieving a remarkable ammonia production rate of 231.3 mmol h^{-1} $g^{-1}_{cat.}$. Through complementary in situ characterizations and computational modeling simulations, we elucidated the active sites and mechanistic investigations governing the NITRR process on **Co-MONTs**. These findings establish critical structure-activity correlations for MONTs-type electrocatalysts, providing a foundation for developing advanced electrocatalytic systems for sustainable chemical synthesis.

Three isostructural MONTs were synthesized through solution-phase chemistry in this work, denoted as: **Fe-MONTs** (*R*-[Fe(pemp)$(H_2O)_2$]), **Co-MONTs** (*R*-[Co(Brpemp)$(H_2O)_2$]), and **Ni-MONTs** (*R*-[Ni(pemp)$(H_2O)_2$]·1/3CH_3CN). For constructing such tubular architectures, we have found that metal phosphonates are particularly suitable due to their kinetic preference for forming stable aqueous-phase structures when combining metal-coordinated amino nitrogen with phosphonate oxygen donors. Structural characterizations reveal the **Co-MONTs** variant possesses a well-defined tubular morphology with 2.17 nm diameter (Figure 1a), constructed from twisted ringlike repeating structural units (Figure 1b,c). The crystalline framework of **Co-MONTs** contains asymmetric units comprising Co centers, $Brpemp^{2-}$ ligands, and coordinated water molecules (Figure S1a). Each Co(II) ion resides in a distorted octahedral environment, bonded to one nitrogen donor and three phosphonate oxygens from separate $Brpemp^{2-}$ ligands, plus two aqua ligands. The framework architecture features [Co-O_5N] octahedra corner-sharing with [P-O_3C] tetrahedra, creating inorganic tube-walls extending along the *c*-axis (Figure S1b). Notably, one coordinated water molecule projects into the pore channel, forming helical hydrogen-bonded chains, while the brominated aromatic groups create a hydrophobic exterior surface—establishing distinct hydrophilic interior and hydrophobic exterior domains (Figure S1c). Topological analysis identifies both Co and P as 3-connected nodes, revealing the tube-walls adopt a graphite-like 6^3 crystal phase. Likewise, **Fe-MONTs** and **Ni-MONTs** exhibit analogous structures (Figure S2), though lacking the incorporation of halogen (−Br) terminal groups present in **Co-MONTs.**

Scanning electron microscopy (SEM) characterization (Figure 2a–c) demonstrates that the synthesized **Co-MONTs** sample exhibits a well-defined tubular structure. Elemental mapping analysis (Figure 2d–k) further reveals uniform spatial

https://doi.org/10.1021/acsmaterialslett.6c00317
ACS Materials Lett. XXXX, XXX, XXX–XXX

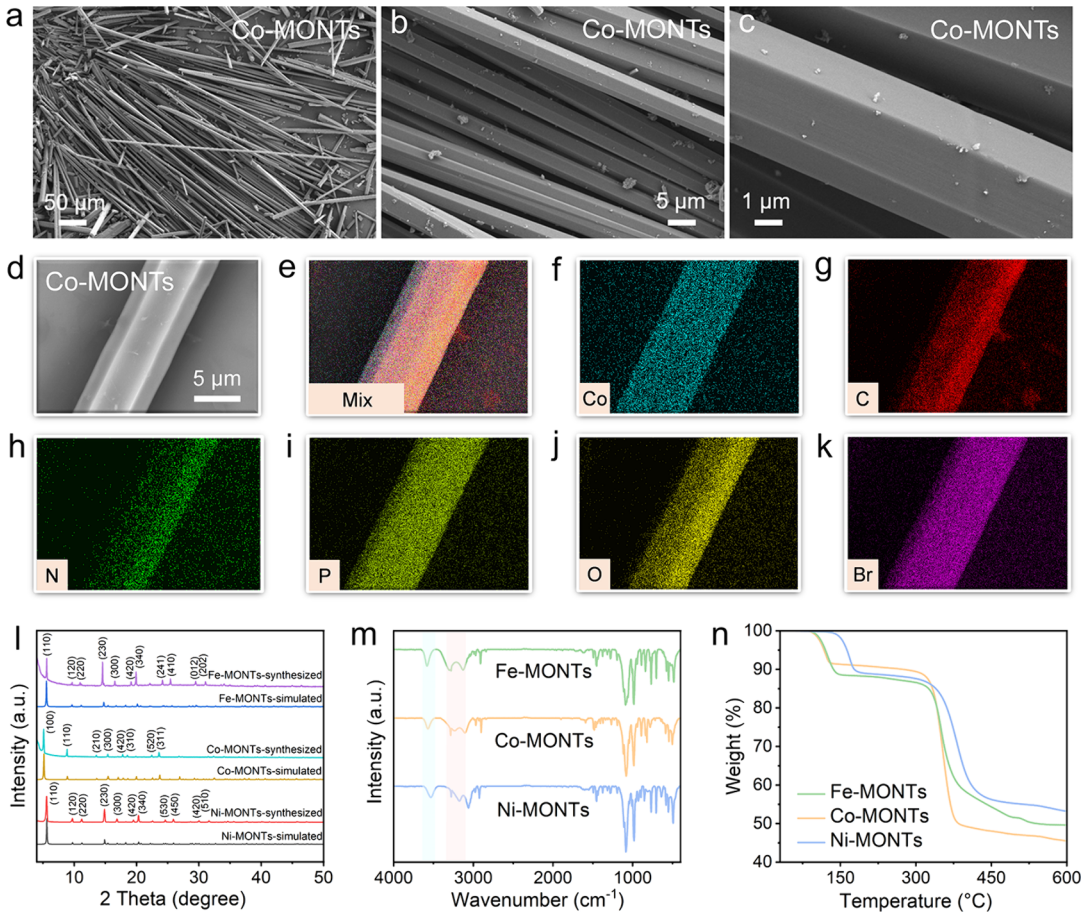

Figure 2. Morphological and structural characterizations of MONTs. (a–c) SEM and (d–k) elemental mapping images of **Co-MONTs** sample, respectively. (l) PXRD patterns, (m) FTIR spectra, and (n) TGA curves of **Fe-MONTs**, **Co-MONTs** and **Ni-MONTs** samples, respectively.

distribution of Co, C, N, P, O, and Br throughout the material. The morphology of the **Fe-MONTs** specimen is presented in the SEM and corresponding elemental mapping images (Figure S3). Meanwhile, the tubular crystalline microstructure of the **Co-MONTs** sample is revealed through both low- and high-resolution transmission electron microscopy (TEM) images (Figure S4). Powder X-ray diffraction (PXRD) analyses confirm the crystalline nature of **Fe-MONTs**, **Co-MONTs** and **Ni-MONTs** samples, with diffraction patterns corresponding to the $P6_3$ hexagonal chiral space group (Figure 2l). While the introduction of bromine substituents in **Co-MONTs** still maintains the overall framework structure, a minor peak shift in the PXRD profile suggests slight lattice expansion due to the larger atomic size of bromine. Complementary Fourier-transform infrared (FTIR) spectroscopic studies (Figure 2m) indicate consistent structural features across all MONTs variants, with characteristic absorption bands observed at ~3600 cm^{-1} (O−H stretching from coordinated water), 3300–3100 cm^{-1} (N−H stretching), and 1100–1000 cm^{-1} (P−O vibrations). Thermal stability evaluation by thermogravimetric analysis (TGA) under N_2 atmosphere shows distinct decomposition profiles for different MONTs samples: **Co-MONTs** exhibits 8.14% mass loss at 85–130 °C, **Fe-MONTs** shows 11.2% loss at 90–142 °C, and **Ni-MONTs** demonstrates 9.74% loss at 130–180 °C (Figure 2n), corresponding to solvent molecule release and subsequent framework degradation upon heating.

X-ray photoelectron spectroscopy (XPS) was employed to examine the surface compositions of **Co-MONTs**. The peaks in Co 2p region (Figure 3a) displays spin-orbit doublets at 781.4 eV ($2p_{3/2}$) and 797.4 eV ($2p_{1/2}$), accompanied by satellite features at ~785.2 and ~802.6 eV.[25,26] The P 2p XPS plot (Figure 3b) shows a single component at 132.8 eV, characteristic of phosphate (P−O) coordination.[27,28] Complementary X-ray absorption near-edge spectroscopy (XANES) at the Co K-edge provided insights into the local coordination environment (Figure 3c). The XANES analysis shows that the edge energy of **Co-MONTs** is close to that of the CoO reference sample, indicating that Co element in **Co-MONTs** has a valence state near +2.[29,30] XANES spectral profiles and their corresponding relative intensities at the K-edge for Co-, Ni-, and Fe-incorporated MONTs are nearly identical (Figure S5), suggesting that these metal elements share equivalent crystallographic positions. This finding aligns with the fundamental principle that XANES features originate from multiple scattering effects occurring within the local atomic environment of the absorber. Fourier-transform extended X-ray absorption fine structure (FT-EXAFS) analysis (Figure 3d) reveals two prominent scattering paths: a primary peak at 1.53 Å (Co−N/O first coordination sphere) and a minor feature at 2.14 Å (attributed to residual Co foil). Quantitative fitting of the first coordination shell (Figure 3e,f and Table S1) yields a six-coordinate environment comprising five Co−O bonds and one Co−N bond,

https://doi.org/10.1021/acsmaterialslett.6c00317
ACS Materials Lett. XXXX, XXX, XXX–XXX

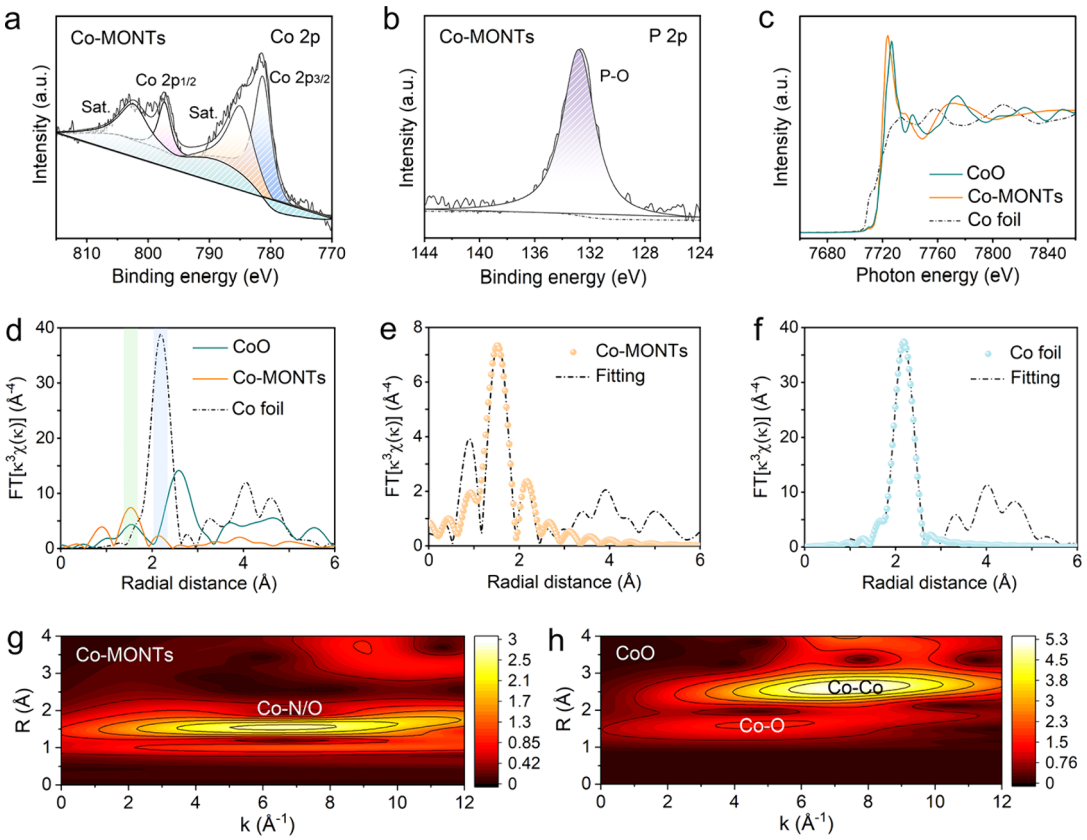

Figure 3. Fine structure characterizations of **Co-MONTs**. (a) XPS spectra at Co 2p level of **Co-MONTs**. (b) XPS spectra at P 2p level of **Co-MONTs**. (c) Co K-edge XANES and (d) FT-EXAFS spectra of **Co-MONTs** compared with reference samples, respectively. (e, f) Co K-edge FT-EXAFS fitting curves of (e) **Co-MONTs** and (f) Co foil, respectively. (g, h) Co K-edge wavelet transformation of (g) **Co-MONTs**, and (h) CoO, respectively.

matching the crystallographic model. Wavelet transform analysis (Figure 3g,h) provides conclusive evidence for Co−N coordination through distinct backscattering patterns in **Co-MONTs** compared to the pure Co−O coordination in CoO reference sample.

The electrocatalytic activities of three M-MONTs (M = Fe, Co, Ni) electrocatalyts for the NITRR were systematically investigated in an H-type cell under ambient conditions. The electrocatalytic performances of the MONTs materials differed markedly, as evidenced by linear sweep voltammetry (LSV) curves recorded in both 0.5 M KNO_3 (Figure 4a) and 0.5 M Na_2SO_4 (Figure S6) solutions. Chronoamperometric measurements at different potentials (Figures S7–S9) demonstrated progressively enhanced current densities with increasing cathodic bias, consistent with potential-dependent small molecule activation. Electrocatalytic performance evaluation showed a clear activity trend: **Co-MONTs** electrode exhibited superior performance to both **Ni-MONTs** and **Fe-MONTs** counterparts (Figure 4b). The **Co-MONTs** achieved peak performance at −0.7 V (vs RHE), delivering a FE_{NH3} of 89.9% and a remarkable NH_3 production rate of 231.3 mmol h^{-1} $g^{-1}_{cat.}$. Comparatively, **Ni-MONTs** and **Fe-MONTs** required higher overpotentials (−0.9 and −0.8 V vs RHE, respectively) to reach their maximum efficiencies of 69.4 and 45.3%. Across various applied potentials, the distribution of nitrogen-containing products from the NITRR on the **Co-MONTs** electrode is illustrated in Figure S10. When tested in a pure 0.5 M KNO_3 electrolyte, only minimal quantities of nitrite (NO_2^-) were observed, suggesting that the conversion of nitrate to ammonia proceeds with high faradaic selectivity. Electrolyte composition studies revealed significant performance dependence on nitrate concentration (Figure S11). The **Co-MONTs** electrocatalyst showed substantially reduced activity in diluted 0.1 M KNO_3–0.1 M Na_2SO_4 electrolyte, as shown in Figure S12. The origin of the ammonia product was confirmed using ^{15}N-labeled nitrate ($Na^{15}NO_3$, 98.3% enriched) as a tracer. In the post-reaction ^{1}H NMR spectrum (Figure S13), a doublet characteristic of $^{15}NH_4^+$ appears, unlike the triplet of $^{14}NH_4^+$ obtained with natural-abundance nitrate. Such distinct isotopic signatures verify that the electrocatalytic ammonia production stems from nitrate reduction, not from unintended nitrogen pollutants.

Stability assessment through extended chronoamperometry (162,000 s) confirmed the good durability of **Co-MONTs** electrode, maintaining stable NH_3 production without noticeable decay of FE_{NH3} (Figure 4c). The **Co-MONTs** electrode was subjected to comprehensive structural characterization before and after extended electrocatalytic operation using a suite of analytical methods. Ex situ Co K-edge XANES spectra (Figure S14) indicated a partial conversion toward a CoO-like state. As shown in Figure S15, the marked reduction in peak intensity for the post-reaction electrode suggests a decrease in the oxidation state of metallic cobalt. Powder X-ray diffraction (Figure S16) further revealed the emergence of an amorphous structure after prolonged electrolysis. Meanwhile, SEM and

https://doi.org/10.1021/acsmaterialslett.6c00317
ACS Materials Lett. XXXX, XXX, XXX–XXX

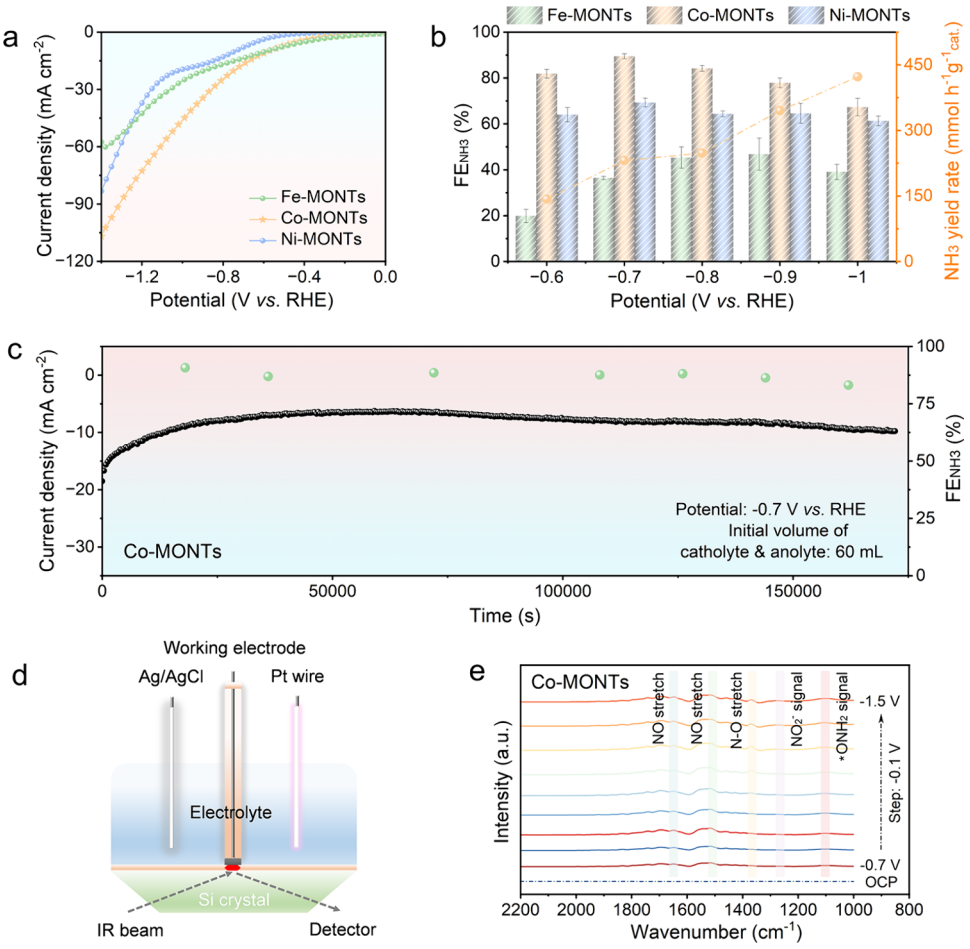

Figure 4. Electrocatalytic activities of MONTs for the NITRR. (a) LSV curves of **Fe-MONTs**, **Co-MONTs** and **Ni-MONTs** electrodes tested in pure 0.5 M KNO_3 electrolyte. (b) FE_{NH3} values (left *Y* axes) and corresponding NH_3 yield rates (right *Y* axes) of **Fe-MONTs**, **Co-MONTs** and **Ni-MONTs** electrodes tested in 0.5 M KNO_3 electrolyte at various applied potentials for the NITRR. (c) Current densities and corresponding FE values of **Co-MONTs** electrode during long-term NITRR stability test at −0.7 V (vs RHE). (d) Schematic illustration of the experimental apparatus for in situ electrochemical ATR-FTIR characterizations. (e) In situ electrochemical ATR-FTIR spectra of **Co-MONTs** electrode under various potentials, respectively.

elemental mapping images (Figures S17 and S18) demonstrated that the **Co-MONTs** electrode underwent only minimal morphological changes following the reaction, providing evidence for its structural robustness. To assess the intrinsic catalytic properties of **Fe-MONTs**, **Co-MONTs**, and **Ni-MONTs** electrodes, their electrochemical surface areas (ECSA) were compared. Cyclic voltammetry (CV) was performed in the potential window from −0.25 to −0.35 V (vs Ag/AgCl), and the double-layer capacitance (C_{dl}) was determined from the slope of the current density difference at −0.30 V plotted against the scan rate. As shown in Figure S19, the derived C_{dl} for **Co-MONTs** (0.55 mF cm^{-2}) is slightly higher than that of **Ni-MONTs** (0.53 mF cm^{-2}) and **Fe-MONTs** (0.32 mF cm^{-2}), suggesting a moderately larger electrochemically active surface area for the **Co-MONTs** catalyst. This elevated capacitance points to improved accessibility of active sites for binding reaction intermediates. Electrochemical impedance spectroscopy (EIS) further differentiated the charge-transfer characteristics of the three electrodes (Figure S20). The Nyquist plots reveal that **Co-MONTs** exhibits a lower charge-transfer resistance (R_{ct}) compared to **Fe-MONTs** and **Ni-MONTs**, indicating more favorable electron transfer kinetics within the **Co-MONTs** electrode.

To elucidate the mechanistic pathways of electrocatalytic NITRR, we conducted in situ attenuated total reflectance Fourier transform infrared (ATR-FTIR) spectroscopy (Figure 4d). The in situ ATR-FTIR spectra of **Co-MONTs** electrocatalyst, obtained under applied potentials ranging from −0.7 to −1.5 V (vs RHE), are presented in Figure 4e. The distinct absorption bands at 1514 and 1648 cm^{-1} correspond to NO stretching vibrations, indicating key deoxygenation events in the reaction pathway.[31,32] A prominent feature at 1370 cm^{-1} arises from nitrate (NO_3^-) stretching, demonstrating its gradual depletion during the electrochemical process.[33,34] Further analyses reveal multiple intermediate species through characteristic infrared absorptions. The band at 1273 cm^{-1} is assigned to the antisymmetric N−O stretching mode of nitrite (NO_2^-), confirming its generation as a nitrate reduction product.[35−37] Additionally, a signal at 1101 cm^{-1} aligns with the −N−O− stretching vibration of $*ONH_2$, a crucial intermediate in ammonia formation.[33,38,39] A weaker absorption near 1460 cm^{-1} matches the σ(N−H) bending of ammonium

https://doi.org/10.1021/acsmaterialslett.6c00317
ACS Materials Lett. XXXX, XXX, XXX−XXX

(NH_4^+), reflecting hydrogenation steps that ultimately yield ammonia.[31,34,40,41] The practical application of the designed metal−organic coordination nanotubes (MONTs) for nitrate reduction reaction (NITRR) hinges on their ability to operate at industrial-scale current densities.[42,43] To evaluate this, a customized flow cell system was developed for electrocatalytic NITRR testing, as shown in Figure S21a. Linear sweep voltammetry (LSV) performed on the **Co-MONTs** electrode in a 0.5 M KNO_3 electrolyte revealed a significant increase in current density compared to that in pure 0.5 M K_2SO_4 electrolyte, indicating the occurrence of NITRR (Figure S21b). Catalytic stability under industrial current is another essential criterion for assessing performance. The **Co-MONTs** electrode was subjected to a chronoamperometry test at −0.8 V (vs RHE) over 10 h in the flow cell setup (Figure S21c). The *I*–*t* profile exhibited a slight decrease after approximately 5 h, suggesting a minor attenuation in catalytic activity. The Faraday efficiency for ammonia production reached 90.2% after 2 h of reaction and remained around 72.7% after 10 h of reaction time.

The electronic structure of the **Co-MONTs** model and its intrinsic relationship with the NITRR were comprehensively investigated through density of states (DOS) analysis. As illustrated in Figure 5a, the HOMO energy level resides at −9.04 eV, with dominant contributions from the d orbitals of Co atoms, followed by the p orbitals of phosphate functional groups, while N-(λ^3-methyl)−1-phenylethan-1-amine (PEA) and −Br ligands exhibit negligible involvement. This electronic configuration unequivocally establishes Co atoms as the primary active centers, dictating the HOMO electron distribution. The localized nature of Co-centered HOMO energy levels creates an electron-rich environment that facilitates the following NITRR process. Further insights into charge redistribution were obtained via electron density difference analysis (Figure 5b), revealing pronounced electron density depletion (cyan regions) around the phosphate groups, while significant electron accumulation (yellow regions) occurs near the Co centers. This phenomenon arises from coordination-induced charge transfer between the organic framework and the metal sites. Additionally, the electrostatic potential (ESP) analysis identified both Co atoms and adjacent water molecules as regions with high ESP values (>90 kcal mol^{-1}), designating them as favorable nucleophilic sites for the NITRR. These electronic and charge distribution features collectively enhance the affinity of **Co-MONTs** toward nitrate adsorption, as corroborated by the interaction profile in Figure 5c, thereby promoting efficient catalytic conversion.

DFT calculations were further performed on the **Co-MONTs** model to construct Gibbs free energy profiles along the NITRR pathway, as presented in Figures S22 and S23. At the Co active site, the binding affinity for a hydrogen proton ($\Delta G^*H = -0.33$ eV) was found to be weaker than that for nitrate ($\Delta G^*NO_3 = -0.52$ eV) (Figure S24), suggesting that the NITRR process is thermodynamically more favorable than the competing HER. Once NO_3^- is adsorbed at the Co site, the resulting $^*NO_3$ species undergoes proton attack to form the $^*HNO_3$ intermediate, an endergonic step requiring 0.27 eV of free energy. The subsequent conversion from $^*HNO_3$ to $^*NO_2$ is exothermic, with a free energy decrease of −1.59 eV. An endothermic step was identified for $^*NO_2 \rightarrow {}^*HNO_2$, involving a free energy increase of 0.61 eV, which thereby serves as the potential determining step (PDS) throughout the catalytic cycle. To further explore possible

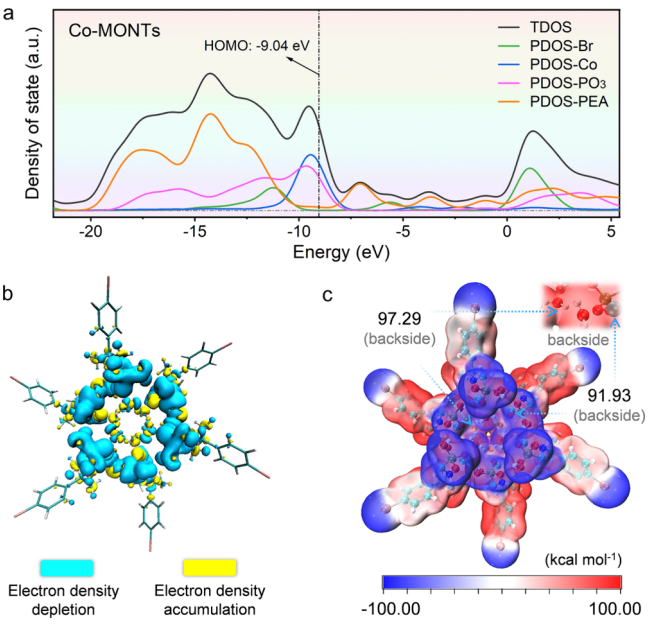

Figure 5. Theoretical calculations. (a) DOS analysis on the **Co-MONTs** model, where N-(λ^3-methyl)−1-phenylethan-1-amine (PEA) corresponds to a minimum structural unit in the **Co-MONTs** model. (b) Electron density difference of NO_3^- adsorbed on the **Co-MONTs** model. The cyan and yellow regions corroborate electron density depletion and electron density accumulation, respectively. (c) ESP surface analysis of the **Co-MONTs** model.

reaction routes, the NO intermediate in both N-end and O-end configurations was also calculated (Figure S22). The hydrogenation of *NO requires a substantial free energy input of 1.60 eV, making it considerably more difficult than that of *ON, which consumes only 0.50 eV. In situ electrochemical ATR-FTIR characterization captured the $^*ONH_2$ intermediate, providing evidence that the NITRR proceeds predominantly via the O-end pathway. Therefore, subsequent analyses focused on this O-end route. Once adsorbed, the *ON intermediate undergoes sequential attack by three H^+/e^- pairs, leading to the formation of *O species along with the release of an NH_3 molecule through exothermic steps. Following that, the *O intermediate is readily reduced to $^*OH_2$ upon further reaction with two additional H^+/e^- pairs at Co sites. Finally, the third H_2O molecule is easily desorbed from the **Co-MONTs** model, completing the catalytic cycle. Consequently, the favorable performance of the **Co-MONTs** model can be ascribed to its preference for NO_3^- adsorption and its ability to lower the energy barrier associated with *NO hydrogenation steps.

In this study, we report the development of a series of MONTs electrocatalysts incorporating diverse metal centers (M = Fe, Co, Ni) and bridging ligands, forming well-defined tubular architectures with atomically dispersed catalytic active sites. These metal-organic coordination polymers (**Fe-MONTs**, **Co-MONTs**, and **Ni-MONTs**) were systematically evaluated for their electrocatalytic performance in the NITRR for ammonia production. Among them, the **Co-MONTs** electrode demonstrated superior catalytic activity, presenting a clear trend in NH_3 production efficiency: Co > Ni > Fe. Under optimized conditions in a pure nitrate electrolyte at −0.7 V (vs RHE), the **Co-MONTs** catalyst achieved a high FE_{NH3} of 89.9% and a remarkable NH_3 yield

https://doi.org/10.1021/acsmaterialslett.6c00317
ACS Materials Lett. XXXX, XXX, XXX−XXX

rate of 231.3 mmol h^{-1} $g^{-1}_{cat.}$, surpassing its Fe and Ni counterparts. Through a combination of in situ spectroscopic investigations and DFT calculations, we elucidated the probable NITRR reaction mechanism and identified the intrinsic catalytic sites within the **Co-MONTs** framework. Notably, the electronic structure analysis reveals Co centers dominate the frontier orbitals, with HOMO (−9.04 eV) electron density primarily localized on Co d-orbitals, leading to superior catalytic predominance. Further charge distribution studies show pronounced electrostatic potential maxima (>90 kcal mol^{-1}) at both metallic Co centers and coordinated water molecules, marking these as preferential locations for nucleophilic attack during the NITRR process. This work highlights the immense potential of tubular MONTs as a versatile catalytic platform, offering insights into the architectural design of advanced electrocatalysts for the sustainable catalytic conversion of small molecules into value-added chemicals.

■ ASSOCIATED CONTENT

Supporting Information

The Supporting Information is available free of charge at https://pubs.acs.org/doi/10.1021/acsmaterialslett.6c00317.

Experimental methods, computational details, crystal structures of MONTs, SEM, TEM, PXRD, LSV curves, *I*−*t* curves, NITRR product selectivity diagram, NITRR activities in lower nitrate concentration, isotope labeling experiments, CV curves, EIS, XANES spectra, EPR spectra, flow cell test, free-energy diagrams in NITRR, optimized geometric structures of reaction intermediates, table of fitted results for the coordination environments of samples, Figures S1−S24, Table S1, and supporting references (DOCX)

■ AUTHOR INFORMATION

Corresponding Authors

Tianyu Shen – *State Key Laboratory of Coordination Chemistry, MOE Key Laboratory of Mesoscopic Chemistry, MOE Key Laboratory of High Performance Polymer Materials and Technology, Jiangsu Key Laboratory of Green Energy Catalysis and Intelligent Chemical Engineering, Suzhou Key Laboratory of Green Intelligent Manufacturing of New Energy Materials and Devices, Tianchang New Materials and Energy Technologies Research Center, Institute of Green Chemistry and Engineering, School of Chemistry and Chemical Engineering, Nanjing University, Nanjing, Jiangsu 210023, P. R. China; School of Chemistry and Chemical Engineering, Suzhou University, Suzhou, Anhui 234000, P. R. China;* Email: 1569695800@qq.com

Zuoxiu Tie – *State Key Laboratory of Coordination Chemistry, MOE Key Laboratory of Mesoscopic Chemistry, MOE Key Laboratory of High Performance Polymer Materials and Technology, Jiangsu Key Laboratory of Green Energy Catalysis and Intelligent Chemical Engineering, Suzhou Key Laboratory of Green Intelligent Manufacturing of New Energy Materials and Devices, Tianchang New Materials and Energy Technologies Research Center, Institute of Green Chemistry and Engineering, School of Chemistry and Chemical Engineering, Nanjing University, Nanjing, Jiangsu 210023, P. R. China;* Email: zxtie@nju.edu.cn

Shuangming Chen – *National Synchrotron Radiation Laboratory, Chinese Academy of Sciences Center for Excellence in Nanoscience, University of Science and Technology of China, Hefei, Anhui 230029, P. R. China;* orcid.org/0000-0001-7567-1552; Email: csmp@ustc.edu.cn

Li-Min Zheng – *State Key Laboratory of Coordination Chemistry, MOE Key Laboratory of Mesoscopic Chemistry, MOE Key Laboratory of High Performance Polymer Materials and Technology, Jiangsu Key Laboratory of Green Energy Catalysis and Intelligent Chemical Engineering, Suzhou Key Laboratory of Green Intelligent Manufacturing of New Energy Materials and Devices, Tianchang New Materials and Energy Technologies Research Center, Institute of Green Chemistry and Engineering, School of Chemistry and Chemical Engineering, Nanjing University, Nanjing, Jiangsu 210023, P. R. China;* orcid.org/0000-0003-4437-1105; Email: lmzheng@nju.edu.cn

Zhong Jin – *State Key Laboratory of Coordination Chemistry, MOE Key Laboratory of Mesoscopic Chemistry, MOE Key Laboratory of High Performance Polymer Materials and Technology, Jiangsu Key Laboratory of Green Energy Catalysis and Intelligent Chemical Engineering, Suzhou Key Laboratory of Green Intelligent Manufacturing of New Energy Materials and Devices, Tianchang New Materials and Energy Technologies Research Center, Institute of Green Chemistry and Engineering, School of Chemistry and Chemical Engineering, Nanjing University, Nanjing, Jiangsu 210023, P. R. China;* orcid.org/0000-0001-8860-8579; Email: zhongjin@nju.edu.cn

Authors

Miao Wang – *State Key Laboratory of Coordination Chemistry, MOE Key Laboratory of Mesoscopic Chemistry, MOE Key Laboratory of High Performance Polymer Materials and Technology, Jiangsu Key Laboratory of Green Energy Catalysis and Intelligent Chemical Engineering, Suzhou Key Laboratory of Green Intelligent Manufacturing of New Energy Materials and Devices, Tianchang New Materials and Energy Technologies Research Center, Institute of Green Chemistry and Engineering, School of Chemistry and Chemical Engineering, Nanjing University, Nanjing, Jiangsu 210023, P. R. China; School of Intelligent Materials and Future Energy, Anhui Normal University, Wuhu, Anhui 241000, P. R. China*

Qian Teng – *State Key Laboratory of Coordination Chemistry, MOE Key Laboratory of Mesoscopic Chemistry, MOE Key Laboratory of High Performance Polymer Materials and Technology, Jiangsu Key Laboratory of Green Energy Catalysis and Intelligent Chemical Engineering, Suzhou Key Laboratory of Green Intelligent Manufacturing of New Energy Materials and Devices, Tianchang New Materials and Energy Technologies Research Center, Institute of Green Chemistry and Engineering, School of Chemistry and Chemical Engineering, Nanjing University, Nanjing, Jiangsu 210023, P. R. China*

Qianchuan Yu – *State Key Laboratory of Coordination Chemistry, MOE Key Laboratory of Mesoscopic Chemistry, MOE Key Laboratory of High Performance Polymer Materials and Technology, Jiangsu Key Laboratory of Green Energy Catalysis and Intelligent Chemical Engineering, Suzhou Key Laboratory of Green Intelligent Manufacturing of New Energy Materials and Devices, Tianchang New Materials and Energy*

Technologies Research Center, Institute of Green Chemistry and Engineering, School of Chemistry and Chemical Engineering, Nanjing University, Nanjing, Jiangsu 210023, P. R. China

Heng Zhou – *National Synchrotron Radiation Laboratory, Chinese Academy of Sciences Center for Excellence in Nanoscience, University of Science and Technology of China, Hefei, Anhui 230029, P. R. China*

Shuaikang Yang – *State Key Laboratory of Coordination Chemistry, MOE Key Laboratory of Mesoscopic Chemistry, MOE Key Laboratory of High Performance Polymer Materials and Technology, Jiangsu Key Laboratory of Green Energy Catalysis and Intelligent Chemical Engineering, Suzhou Key Laboratory of Green Intelligent Manufacturing of New Energy Materials and Devices, Tianchang New Materials and Energy Technologies Research Center, Institute of Green Chemistry and Engineering, School of Chemistry and Chemical Engineering, Nanjing University, Nanjing, Jiangsu 210023, P. R. China*

Huaizhu Wang – *State Key Laboratory of Coordination Chemistry, MOE Key Laboratory of Mesoscopic Chemistry, MOE Key Laboratory of High Performance Polymer Materials and Technology, Jiangsu Key Laboratory of Green Energy Catalysis and Intelligent Chemical Engineering, Suzhou Key Laboratory of Green Intelligent Manufacturing of New Energy Materials and Devices, Tianchang New Materials and Energy Technologies Research Center, Institute of Green Chemistry and Engineering, School of Chemistry and Chemical Engineering, Nanjing University, Nanjing, Jiangsu 210023, P. R. China*

Zuoao Wu – *State Key Laboratory of Coordination Chemistry, MOE Key Laboratory of Mesoscopic Chemistry, MOE Key Laboratory of High Performance Polymer Materials and Technology, Jiangsu Key Laboratory of Green Energy Catalysis and Intelligent Chemical Engineering, Suzhou Key Laboratory of Green Intelligent Manufacturing of New Energy Materials and Devices, Tianchang New Materials and Energy Technologies Research Center, Institute of Green Chemistry and Engineering, School of Chemistry and Chemical Engineering, Nanjing University, Nanjing, Jiangsu 210023, P. R. China*

Complete contact information is available at: https://pubs.acs.org/doi/10.1021/acsmaterialslett.6c00317

Author Contributions

[#]M.W., Q.T., Q.Y., and H.Z. contributed equally to this work.

Notes

The authors declare no competing financial interest.

■ ACKNOWLEDGMENTS

This work was supported by the National Natural Science Foundation of China (U25A20628, 22561160129, 22479074, and 22475096), the Equipment Pre-Research and Ministry of Education Joint Fund (8091B02052407), the Fundamental Research Program Key Project of Jiangsu Province (BK20253008), the Science and Technology Major Project of Jiangsu Province (BG2024013), the Scientific and Technological Achievements Transformation Special Fund of Jiangsu Province (BA2023037), the Academic Degree and Postgraduate Education Reforming Project of Jiangsu Province (JGKT24_C001), the Key Core Technology Open Competition Project of Suzhou City (SYG2024122), the Open Research Fund of Suzhou Laboratory (SZLAB-1308-2024-TS005), the Chenzhou National Sustainable Development Agenda Innovation Demonstration Zone Provincial Special Open Competition Project (2023sfq11, 2025sfq38), and the Fundamental Research Funds for the Central Universities and Nanjing University International Collaboration Initiative (020514380354).

■ REFERENCES

(1) Tang, C.; Qiao, S. Z. How to Explore Ambient Electrocatalytic Nitrogen Reduction Reliably and Insightfully. *Chem. Soc. Rev.* **2019**, *48*, 3166−3180.

(2) Good, A. Toward Nitrogen-Fixing Plants. *Science* **2018**, *359*, 869−870.

(3) Shi, R.; Zhang, X.; Waterhouse, G.; Zhao, X.; Zhang, R. The Journey toward Low Temperature, Low Pressure Catalytic Nitrogen Fixation. *Adv. Energy Mater.* **2020**, *10*, 2000659.

(4) Zhang, J.; Tian, X.; Liu, M.; Guo, H.; Zhou, J.; Fang, Q.; Liu, Z.; Wu, Q.; Lou, J. Cobalt-Modulated Molybdenum−Dinitrogen Interaction in MoS_2 for Catalyzing Ammonia Synthesis. *J. Am. Chem. Soc.* **2019**, *141*, 19269−19275.

(5) Hui, L.; Xue, Y.; Yu, H.; Liu, Y.; Fang, Y.; Xing, C.; Huang, B.; Li, Y. Highly Efficient and Selective Generation of Ammonia and Hydrogen on a Graphdiyne-Based Catalyst. *J. Am. Chem. Soc.* **2019**, *141*, 10677−10683.

(6) Zhang, L.; Ding, L.; Chen, G.; Yang, X.; Wang, H. Ammonia Synthesis under Ambient Conditions: Selective Electroreduction of Dinitrogen to Ammonia on Black Phosphorus Nanosheets. *Angew. Chem., Int. Ed.* **2019**, *131*, 2638−2642.

(7) Li, S.; Bao, D.; Shi, M.; Wulan, B.; Yan, J.; Jiang, Q. Amorphizing of Au Nanoparticles by CeO_x-RGO Hybrid Support towards Highly Efficient Electrocatalyst for N_2 Reduction under Ambient Conditions. *Adv. Mater.* **2017**, *29*, 1700001.

(8) Jiang, M.; Han, L.; Peng, P.; Hu, Y.; Xiong, Y.; Mi, C.; Tie, Z.; Xiang, Z.; Jin, Z. Quasi-Phthalocyanine Conjugated Covalent Organic Frameworks with Nitrogen-Coordinated Transition Metal Centers for High-Efficiency Electrocatalytic Ammonia Synthesis. *Nano Lett.* **2022**, *22*, 372−379.

(9) Gao, Q.; Pillai, H. S.; Huang, Y.; Liu, S.; Mu, Q.; Han, X.; Yan, Z.; Zhou, H.; He, Q.; Xin, H.; Zhu, H. Breaking Adsorption-Energy Scaling Limitations of Electrocatalytic Nitrate Reduction on Intermetallic CuPd Nanocubes by Machine-Learned Insights. *Nat. Commun.* **2022**, *13*, 2338.

(10) Liu, C.; Zhang, G.; Zhang, W.; Gu, Z.; Zhu, G. Specifically Adsorbed Ferrous Ions Modulate Interfacial Affinity for High-Rate Ammonia Electrosynthesis from Nitrate in Neutral Media .*Proc. Natl. Acad. Sci. U. S. A.* **2023**, *120*, e2209979120.

(11) Lv, Y.; Ke, S.-W.; Gu, Y.; Tian, B.; Tang, L.; Ran, P.; Zhao, Y.; Ma, J.; Zuo, J.-L.; Ding, M. Highly Efficient Electrochemical Nitrate Reduction to Ammonia in Strong Acid Conditions with Fe_2M-Trinuclear-Cluster Metal−Organic Frameworks. *Angew. Chem., Int. Ed.* **2023**, *62*, e202305246.

(12) Langevelde, P. H.; Katsounaros, I.; Koper, M. T. M. Electrocatalytic Nitrate Reduction for Sustainable Ammonia Production. *Joule* **2021**, *5*, 290−294.

(13) Zhang, Z.; Lv, Y.; Gu, Y.; Zhou, X.; Tian, B.; Zhang, A.; Yang, Z.; Chen, S.; Ma, J.; Ding, M.; Zuo, J.-L. Dual Zn_5-NiS_4 Sites in a Redox-Active Metal−Organic Framework Enables Efficient Cascade Catalysis for Nitrate-to-Ammonia Conversion. *Angew. Chem., Int. Ed.* **2024**,*64*, e202418272.

(14) Zhang, R.; Hong, H.; Liu, X.; Zhang, S.; Li, C.; Cui, H.; Wang, Y.; Liu, J.; Hou, Y.; Li, P.; Huang, Z.; Guo, Y.; Zhi, C. Molecular Engineering of a Metal−Organic Polymer for Enhanced Electrochemical Nitrate-to-Ammonia Conversion and Zinc Nitrate Batteries. *Angew. Chem., Int. Ed.* **2023**, *62*, e202309930.

(15) Wang, Y.; Sun, M.; Zhou, J.; Xiong, Y.; Zhang, Q.; Yee, C.; Wang, X.; Lu, P.; Feng, T.; Hao, F.; Liu, F.; Wang, J.; Ma, Y.; Yin, J.; Chu, S.; Gu, L.; Huang, B.; Fan, Z. Atomic Coordination Environment Engineering of Bimetallic Alloy Nanostructures for Efficient Ammonia Electrosynthesis from Nitrate. *Proc. Natl. Acad. Sci. U. S. A.* **2023**, *120*, e2306461120.

(16) Liu, F.; Zhou, J.; Sun, M.; Xu, Z.; Wang, H.; Yao, N.; Wang, Y.; Hao, F.; Xiong, Y.; Wang, J.; Guo, L.; Wa, Q.; Wang, G.; Meng, X.; Shao, M.; Wang, C.; Chen, H.-C.; Chen, H. M.; Zhu, Y.; Huang, B.; Fan, Z. Enhanced p−d Orbital Coupling in Unconventional Phase RhSb Alloy Nanoflowers for Efficient Ammonia Electrosynthesis in Neutral Media. *Angew. Chem., Int. Ed.* **2025**, *137*, e202504641.

(17) Chen, F.; Zhou, X.; Wang, H.; Liu, X.; Yang, Q.; Chen, X.; Mu, Q.; Liu, J.; Li, X.; Liao, X.; Jiang, Z.; Jin, Z.; Jiang, M. Bidirectional Nitrogen Neutralization via Coupled Electrocatalytic Processes of Nitrate Reduction and Hydrazine Oxidation. *Adv. Funct. Mater.* **2025**, *35*, 2421405.

(18) Wang, Y.; Hao, F.; Xu, H.; Sun, M.; Wang, X.; Xiong, Y.; Zhou, J.; Liu, F.; Hu, Y.; Ma, Y.; Meng, X.; Guo, L.; Wang, J.; Lu, P.; Yin, J.; Wang, J.; Niu, W.; Ye, C.; Zhang, Q.; Xi, S.; Huang, B.; Shao, M.; Fan, Z. Interfacial Water Structure Modulation on Unconventional Phase Non-Precious Metal Alloy Nanostructures for Efficient Nitrate Electroreduction to Ammonia in Neutral Media. *Angew. Chem., Int. Ed.* **2025**, *137*, e202508617.

(19) Xie, L. S. Electrically Conductive Metal−Organic Frameworks. *Chem. Rev.* **2020**, *120*, 8536−8580.

(20) Yang, Q.; Xu, Q.; Jiang, H.-L. Metal−Organic Frameworks Meet Metal Nanoparticles: Synergistic Effect for Enhanced Catalysis. *Chem. Soc. Rev.* **2017**, *46*, 4774−4808.

(21) Jiao, L.; Wang, Y.; Jiang, H.-L.; Xu, Q. Metal−Organic Frameworks as Platforms for Catalytic Applications. *Adv. Mater.* **2018**, *30*, 1703663.

(22) Xiong, Y.; Li, B.; Gu, Y.; Yan, T.; Ni, Z.; Li, S.; Zuo, J.; Ma, J.; Jin, Z. Photocatalytic Nitrogen Fixation under an Ambient Atmosphere Using a Porous Coordination Polymer with Bridging Dinitrogen Anions. *Nat. Chem.* **2023**, *15*, 286−293.

(23) Jia, J.-G.; Zhao, C.-C.; Bao, S.-S.; Wu, L.-Q.; Wen, G.-H.; Jacobson, A. J.; Ma, J.; Zheng, L.-M. Layer or Tube? Uncovering Key Factors Determining the Rolling-Up of Layered Coordination Polymers. *J. Am. Chem. Soc.* **2021**, *143*, 17587−17598.

(24) Wang, M.; Meng, Y.-R.; Xu, W.; Shen, T.; Wang, Y.; Yu, Q.; Liu, C.; Gu, Y.; Tie, Z.; Fan, Z.; Zuo, J.-L.; Su, J.; Jin, Z. Square-Planar Tetranuclear Cluster-Based High-Symmetry Coordination Metal−Organic Polymers for Efficient Electrochemical Nitrate Reduction to Ammonia. *J. Am. Chem. Soc.* **2025**, *147*, 18327−18337.

(25) Sun, L.; Reddu, V.; Xi, S.; Dai, C.; Sheng, Y.; Su, T.; Fisher, A. C.; Wang, X. Cobalt Quaterpyridine Complexes for Highly Efficient Heterogeneous CO_2 Reduction in Aqueous Media. *Adv. Energy Mater.* **2022**, *12*, 2202108.

(26) Wang, M.; Li, S.; Gu, Y.; Xu, W.; Wang, H.; Sun, J.; Chen, S.; Tie, Z.; Zuo, J.; Ma, J.; Su, J.; Jin, Z. Polynuclear Cobalt Cluster-Based Coordination Polymers for Efficient Nitrate-to-Ammonia Electroreduction. *J. Am. Chem. Soc.* **2024**, *146*, 20439−20448.

(27) Guo, X.; Zhang, W.; Zhang, J.; Zhou, D.; Tang, X.; Xu, X.; Li, B.; Liu, H.; Wang, G. Boosting Sodium Storage in Two-Dimensional Phosphorene/$Ti_3C_2T_x$ MXene Nanoarchitectures with Stable Fluorinated Interphase. *ACS Nano* **2020**, *14*, 3651−3659.

(28) Xing, H.; He, W.; Liu, Y.; Long, G.; Sun, Y.; Feng, J.; Feng, W.; Zhou, Y.; Zong, Y.; Li, X.; Zhu, X.; Zheng, X. Ultrathin and Highly Crumpled/Porous CoP Nanosheet Arrays Anchored on Graphene Boosts the Capacitance and Their Synergistic Effect toward High-Performance Battery-Type Hybrid Supercapacitors. *ACS Appl. Mater. Interfaces* **2021**, *13*, 26373−26383.

(29) Haandel, L.; Smolentsev, G.; Bokhoven, J.; Hensen, E.; Weber, T. Evidence of Octahedral Co−Mo−S Sites in Hydrodesulfurization Catalysts as Determined by Resonant Inelastic X-Ray Scattering and X-Ray Absorption Spectroscopy. *ACS Catal.* **2020**, *10*, 10978−10988.

(30) Tang, P.; Gao, P.; Cui, X.; Chen, Z.; Fu, Q.; Wang, Z.; Mo, Y.; Liu, H.; Xu, C.; Liu, J.; Yan, J.; Passerini, S. Covalency Competition Induced Active Octahedral Sites in Spinel Cobaltites for Enhanced Pseudocapacitive Charge Storage. *Adv. Energy Mater.* **2022**, *12*, 2102053.

(31) Song, Z.; Liu, Y.; Zhong, Y.; Guo, Q.; Zeng, J.; Geng, Z. Efficient Electroreduction of Nitrate into Ammonia at Ultralow Concentrations via an Enrichment Effect. *Adv. Mater.* **2022**, *34*, e2204306.

(32) Bae, S.-E.; Stewart, K. L.; Gewirth, A. A. Nitrate Adsorption and Reduction on Cu(100) in Acidic Solution. *J. Am. Chem. Soc.* **2007**, *129*, 10171−10180.

(33) Fang, J.; Zheng, Q.-Z.; Lou, Y.-Y.; Zhao, K.-M.; Hu, S.-N.; Li, G.; Akdim, O.; Huang, X.-Y.; Sun, S.-G. Ampere-Level Current Density Ammonia Electrochemical Synthesis Using CuCo Nanosheets Simulating Nitrite Reductase Bifunctional Nature. *Nat. Commun.* **2022**, *13*, 7899.

(34) Zhang, N.; Shang, J.; Deng, X.; Cai, L.; Long, R.; Xiong, Y.; Chai, Y. Governing Interlayer Strain in Bismuth Nanocrystals for Efficient Ammonia Electrosynthesis from Nitrate Reduction. *ACS Nano* **2022**, *16*, 4795−4804.

(35) Figueiredo, M. C.; Solla-Gullón, J.; Vidal-Iglesias, F. J.; Climent, V.; Feliu, J. M. Nitrate Reduction at Pt(100) Single Crystals and Preferentially Oriented Nanoparticles in Neutral Media. *Catal. Today* **2013**, *202*, 2−11.

(36) Hao, R.; Tian, L.; Wang, C.; Wang, L.; Liu, Y.; Wang, G.; Li, W.; Ozin, G. A. Pollution to Solution: A Universal Electrocatalyst for Reduction of All NO_x-Based Species to NH_3. *Chem. Catal.* **2022**, *2*, 622−638.

(37) Figueiredo, M. C.; Souza-Garcia, J.; Climent, V.; Feliu, J. M. Nitrate Reduction on Pt(111) Surfaces Modified by Bi Adatoms. *Electrochem. Commun.* **2009**, *11*, 1760−1763.

(38) Pérez-Gallent, E.; Figueiredo, M. C.; Katsounaros, I.; Koper, M. T. M. Electrocatalytic Reduction of Nitrate on Copper Single Crystals in Acidic and Alkaline Solutions. *Electrochim. Acta* **2017**, *227*, 77−84.

(39) Rosca, V.; Beltramo, G. L.; Koper, M. T. M. Hydroxylamine Electrochemistry at Polycrystalline Platinum in Acidic Media: A Voltammetric, DEMS and FTIR Study. *J. Electroanal. Chem.* **2004**, *566*, 53−62.

(40) Li, S.; Pang, Y.; Li, H.; Yang, R.; Jin, Z.; Yu, G.; Li, P. Cross-Scale Understanding of Cascade Electrocatalysis for Carbon and Nitrogen Utilization. *Chem. Sci.* **2026**, *17*, 772.

(41) Zhang, Y.; Zheng, H.; Zhou, K.; Ye, J.; Chu, K.; Zhou, Z.; Zhang, L.; Liu, T. Conjugated Coordination Polymer as a New Platform for Efficient and Selective Electroreduction of Nitrate into Ammonia. *Adv. Mater.* **2023**, *35*, 2209855.

(42) Wang, P.; Li, P.; Pan, Z.; Liu, K.; Xie, M.; Zhou, L.; Zhou, M.; Yu, G.; Jin, Z. Photothermal-Electrocatalysis Interface for Fuel-Cell Grade Ammonia Harvesting from the Environment. *Nat. Commun.* **2025**, *16*, 5581.

(43) Yi, M.; Wang, P.; Shi, R.; Guo, W.; Yang, D.; Li, P.; Yu, G.; Jin, Z. Pulse-Electrodeposited Single-Atom Alloys with Steered Surface Hydrogenation Dynamics for Air-to-Fertilizer Synthesis. *Angew. Chem., Int. Ed.* **2026**, *65*, e21345.

https://doi.org/10.1021/acsmaterialslett.6c00317
ACS Materials Lett. XXXX, XXX, XXX−XXX